3-D Microvascular Imaging Using High Frame Rate Ultrasound and ASAP Without Contrast Agents: Development and Initial *In Vivo* Evaluation on Nontumor and Tumor Models

Chee Hau Leow[ID], Nigel L. Bush, Antonio Stanziola, Marta Braga, Anant Shah, Javier Hernández-Gil, Nicholas J. Long, Eric O. Aboagye, Jeffrey C. Bamber, and

Meng-Xing Tang[ID], *Senior Member, IEEE*

Abstract—Three-dimensional imaging is valuable to noninvasively assess angiogenesis given the complex 3-D architecture of vascular networks. The emergence of high frame rate (HFR) ultrasound, which can produce thousands of images per second, has inspired novel signal processing techniques and their applications in structural and functional imaging of blood vessels. Although highly sensitive vascular mapping has been demonstrated using ultrafast Doppler, the detectability of microvasculature from the background noise may be hindered by the low signal-to-noise ratio (SNR) particularly in the deeper region and without the use of contrast agents. We have recently demonstrated a coherence-based technique, acoustic subaperture imaging (ASAP), for super-contrast vascular imaging and illustrated the contrast improvement using HFR contrast-enhanced ultrasound. In this work, we provide a feasibility study for microvascular imaging using ASAP without contrast agents, and extend its capability from 2-D to volumetric vascular mapping. Using an ultrasound research system and a preclinical probe, we demonstrated the improved visibility of microvascular mapping using ASAP in comparison to ultrafast power Doppler (PD) on a mouse kidney, liver, and tumor without contrast agent injection. The SNR of ASAP images improves in average by 10 dB when compared to PD. In addition, directional velocity mappings were also demonstrated by combining ASAP with the phase information extracted from lag-1 autocorrelation. The 3-D vascular and velocity mapping of the mouse kidney, liver, and tumor were demonstrated by stacking the ASAP images acquired using 2-D ultrasound imaging and a trigger-controlled linear translation stage. The 3-D results depicted clear microvasculature morphologies and functional information in terms of flow direction and velocity in two nontumor models and a tumor model. In conclusion, we have demonstrated a new 3-D *in vivo* ultrasound microvascular imaging technique with significantly improved SNR over existing ultrafast Doppler.

Index Terms—Doppler, microvascular flow, noise reduction, spatio-temporal coherence analysis, volumetric imaging.

I. INTRODUCTION

ANGIOGENESIS is an important predictor of both normal physiological processes and biological behavior of many diseases [1]–[3]. The early identification of the vascular changes by means of noninvasive imaging has become invaluable to detect early vascular changes associated with tumor progression, differentiate benign from malignant masses, and monitor the response to treatment. Existing flow imaging modalities that are able to visualize tumor vascular environment include computed tomography (CT), magnetic resonance imaging (MRI), and ultrasound imaging. Both CT and MRI have the advantages of full-3-D volumetric imaging and reasonable spatial resolution, although the long acquisition time and relatively high cost result in a lack of accessibility. CT is also less preferential than other imaging modalities, predominantly due to the use of ionizing radiation. Ultrasound, on the other hand, is portable and affordable. It has the highest temporal resolution among these modalities, high and scalable spatial resolution, and the capability for real-time imaging making ultrasound an indispensable tool for frontline clinical use.

The conventional Doppler ultrasound imaging can be used to detect large vessels with relatively fast blood flow [4], [5]. The Doppler processing allows flow information to be extracted by high-pass frequency filtering and low-pass amplitude thresholding of the frequency demodulated signal, to suppress Doppler signal clutter that comes from moving solid tissue, and ensemble averaging of the Doppler signals to reduce noise. The low imaging frame rate of a conventional ultrasound and the tissue movement (tens of hertz), however, makes it difficult to fully eliminate clutter due to tissue

C. H. Leow, A. Stanziola, and M.-X. Tang are with the Department of Bioengineering, Imperial College London, London SW7 2AZ, U.K. (e-mail: c.leow12@imperial.ac.uk; mengxing.tang@imperial.ac.uk).

N. L. Bush and J. C. Bamber are with the Joint Department of Physics and Cancer Research UK Cancer Imaging Centre, The Institute of Cancer Research and Royal Marsden NHS Foundation Trust, London, U.K.

M. Braga and E. O. Aboagye are with the Comprehensive Cancer Imaging Centre, Department of Surgery and Cancer, Imperial College London SM2 5NG, London, U.K.

A. Shah was with the Joint Department of Physics and Cancer Research UK Cancer Imaging Centre, The Institute of Cancer Research and Royal Marsden NHS Foundation Trust, London, U.K. He is now with Ultrasound and Underwater Acoustics, National Physical Laboratory, Teddington TW110LW, U.K.

J. Hernández-Gil and N. J. Long are with the Comprehensive Cancer Imaging Centre, Department of Surgery and Cancer, Imperial College London, London SM2 5NG, U.K., and also with the Department of Chemistry, Imperial College London, London SW7 2AZ, U.K.

This paper has supplementary downloadable material at http://ieeexplore.ieee.org, provided by the authors.
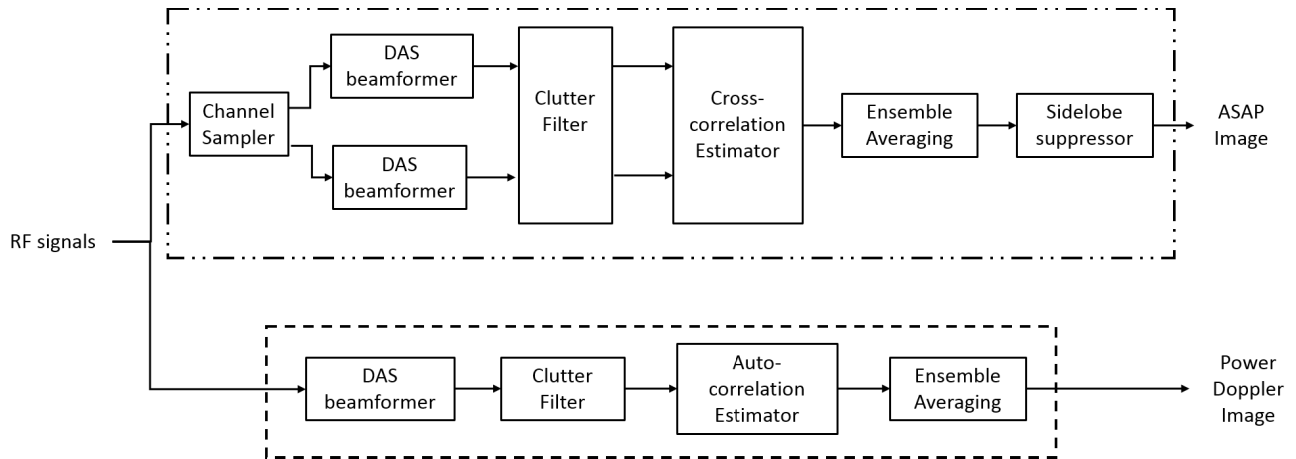
Fig. 1. Alternative signal processing paths of PD and ASAP imaging.

motion. Furthermore, limited ensemble length of the conventional Doppler signals also results in poor sensitivity to the slow flow in the microvascular environment. For this reason, contrast-enhanced ultrasound (CEUS) has been established to enhance the flow signal for microvascular imaging. In CEUS, microbubble contrast agents are injected into the blood stream and used in combination with pulse-sequences and matching signal processing to detect the nonlinear properties of microbubble echoes and thus increase the sensitivity and specificity of microvessel detection and to the flow signal. Several techniques have been developed, including nonlinear contrast imaging [6]–[9], nonlinear Doppler [10], acoustic angiography [11], and acoustic super-resolution [12], [13]. This increase in sensitivity to small vessels and slow blood flow is particularly beneficial for the assessment of angiogenesis in the tumor microenvironment.

Recent advancements of high frame rate (HFR) ultrasound further enhance the capabilities of ultrasound for blood flow quantification [14]–[19], potentially offering visualization of microvasculature with and without the need to inject microbubbles. The high temporal resolution not only can be used to better visualize and quantify fast moving objects but can also be traded to substantially improve the sensitivity of Doppler ultrasound given the use of longer Doppler ensemble averaging [14], [19], [20]. The high frame rate imaging also facilitates better clutter rejection techniques such as eigendecomposition-based clutter filter [21], [22]. The power Doppler (PD) technique further improves Doppler signal-to-noise (SNR) ratio by integrating over all Doppler shift frequencies, sacrificing frequency-shift information to improve sensitivity. It is still, however, bounded by the limitation where ensemble averaging reduces the noise power variance but not the mean of the noise background. As the signal reduces with depth, it poses a great challenge to distinguish smaller vessels from the noise background particularly in the deeper regions and for noncontrast imaging.

Several techniques have been developed to reduce the noise background in ultrafast PD images, include the following. Song *et al.* [23] implemented a block-wise singular value decomposition (SVD) filter to locally reject both clutter and noise with the tradeoff of significantly increased computa-

tional cost. Tremblay-Darveau *et al.* [24] exploited the temporal (slow time) signal coherence and showed promising noise suppression by imaging of the first-lag rather than the zeroth-lag statistic of the autocorrelation function. However, the higher lags may suffer from aliasing, and decorrelation of the slow-time signals during coherent compounding may reduce the SNR. Li and Dahl [25] showed that the noise is uncorrelated between channels and proposed a spatial coherence beamforming technique to reduce the noise background and enhance the Doppler sensitivity. Although promising results have been demonstrated, this method is computationally demanding and/or may suffer from spatial blurring.

We recently developed acoustic subaperture processing (ASAP) for super-contrast vasculature imaging, and demonstrated its feasibility for improving 2-D HFR-CEUS imaging [26], [27]. In this study, we aim to demonstrate the applicability of ASAP for improving the quality of volumetric microvascular images acquired without the use of contrast agents. A mechanically swept linear array was used to acquire volumetric data. To facilitate comparison with ultrafast Doppler, the image quality improvement is assessed in terms of contrast and visibility of the smallest vessels seen in two nontumors and a tumor mouse model. Corresponding volumetric vascular mappings and directional velocity mappings are demonstrated.

II. METHODS

A. Power Doppler Versus Acoustic Subaperture Processing

The outline of the signal processing steps of PD and ASAP is shown in Fig. 1. Starting from the channel data acquired from an HFR ultrasound system, an ultrasound image can be reconstructed by delay-and-sum (DAS) applied to the radio frequency (RF) signal across the receive aperture with M elements. While the reconstructed RF images contain both blood and clutter signals, an SVD-based filter is applied to differentiate the flow signal from the tissue signal. A PD image is then produced by ensemble averaging the power signal output from the well-established autocorrelation estimator [4], [5]

$$\text{PD} = \sum_{t=1}^{T} |s(n,t)s^*(n,t)| \qquad (1)$$

where s is the clutter-filtered complex signal, n is the fast time (spatial location) sample index, and t is the slow time (temporal) sample index. $*$ denotes the complex conjugate, and $|-|$ denotes the modulus operator.

ASAP was developed to reduce the noise in PD images by assuming that the noise between channels is uncorrelated [26]. With the same receive channel data, two set of images were reconstructed by splitting the channels into two nonoverlapping subapertures with noncommon elements. This can be thought as having a channel sampler which selects the channel data for each beamformer or having two complementary receive apodizations to form two images from the same RF data. Given that M channel data have been received, one could possibly form the two subapertures ($M/2$ channels for each subaperture) by using the odd and even channels as two separate groups. This, however, may cause grating lobes to appear in the images as the pitch of the sampling of the new subaperture increases by twofold. To reduce this problem, the subapertures can be formed by alternating the channel sampler after every four elements, as previously discussed in [26].

Subsequently, SVD clutter filtering was performed to extract the blood signal from both of the reconstructed subaperture RF images before applying a cross-correlation estimator. The cross-correlator can be described as

$$R = \sum_{t=1}^{T} s_1(n, t)s_2^*(n, t) \tag{2}$$

where R is the complex cross-correlated signal, s_1 and s_2 are the clutter-filtered complex signals from the two subapertures, n is the fast time sample index, t is the slow-time sample index, and $*$ is the complex conjugate operator. Note that since part of the noise in the two-independent apertures is uncorrelated, the SNR increases as the noise is reduced but the coherent flow signal remains. This is fundamentally different from PD, in which a single aperture is used and the correlated noise signals contribute to the final power signal.

While the output from the cross-correlation estimator is a complex scalar, the phase information can be used to reduce the off-axis signals such as grating lobes and sidelobes. It should also be noted that beamforming images using a subaperture with increased pitch between elements will also create grating lobes. However, because the two subapertures are independent of each other, the grating lobes will form in such a way that they are 180° out-of-phase with each other [28]. Here, a weight vector determined by the phase of the correlated signal is applied to suppress the off-axis signal

$$\text{ASAP}(n, t) = |R|e^{-\left(\frac{k^2}{k_0^2}\right)} \tag{3}$$

where k denotes the phase angle of the sample, and k_o is empirically determined so as to attenuate out-of-phase signals at $\pi/3$.

In order to determine the flow direction and velocity, ASAP imaging can be combined with the lag-1 autocorrelation to extract the velocity information. A binary vessel mask, defined using the power amplitude from the ASAP, is multiplied
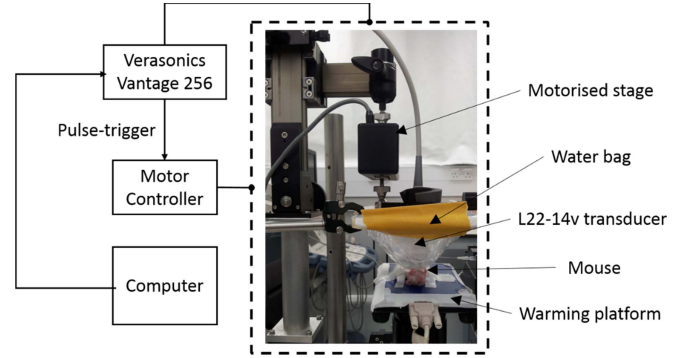

Fig. 2. Experimental setup of the 3-D imaging system. A mouse is placed under a water bag, and the transducer is moved freely in a water bag using a linear motorized stage synchronized with a HFR ultrasound system.

with the directional flow velocity computed from the phase information extracted from the lag-1 autocorrelation.

B. Animal Model

In vivo studies were conducted on three female athymic nude mice: two nontumor-bearing mice and a tumor-bearing mouse. All procedures complied with the Animal Act 1986 and were approved by the Animal Welfare and Ethical Review Body of the Institute of Cancer Research. The tumor in the tumor-bearing mouse was grown by implanting SW620 colon adenocarcinoma cells subcutaneously in the right flank region. Imaging took place when the tumor had grown to a size of approximately 1 cm in each axis. For the nontumor-bearing mouse, the kidney of the mouse was imaged.

C. 3-D Imaging and Imaging Protocol

The experimental setup is shown in Fig. 2. During the experiment, the mouse was anesthetized by subcutaneous injection of Fentanyl citrate + Fluanisone (Hypnorm) and Midazolam (Hypnovel) (0.28:10: 4.5 mg/kg) before placing the animal on a warming platform to regulate its temperature. The ultrasound gel was applied to couple the mouse skin with a polyethylene bag containing water. The probe was placed in the water bag so that it could move freely without affecting the position of the mouse during volumetric data acquisition.

Imaging was performed using a Verasonics Vantage system (Verasonics Inc., Redmond, WA, USA) and a L22-14v linear probe. A stepper motor was synchronized with this system to move the transducer along the elevation direction with a step size between 150 and 400 μm and to cover the volume of interest, between 8 and 10 mm. For each imaging plane, 1500 coherent compounded plane wave images were collected at an effective frame rate of 500 Hz. To form an image, fifteen 1-cycle pulses were transmitted at the center frequency of 18 MHz, each pulse generating plane waves at a different angle in 1° increments within a 15° range (−7° to 7°). The same RF data were used in postprocessing to reconstruct both Doppler and ASAP images. Although a multicycle pulse would be beneficial for Doppler, especially for velocity imaging, 1-cycle pulse was chosen such that the highest possible spatial resolution for the final vasculature images can be preserved while sacrificing some velocity resolution. The MI
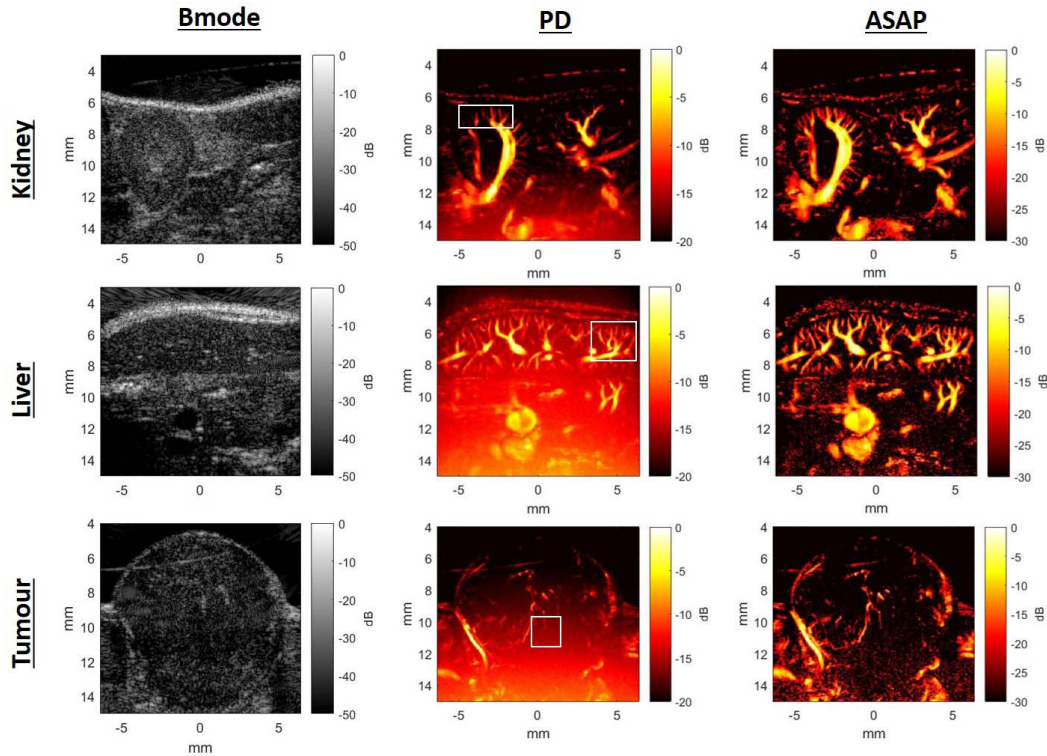
Fig. 3. 2-D comparison of the B-mode, PD, and ASAP images of a kidney model (top row), a liver model (middle row), and a tumor model (bottom row). Note that all images are acquired in the middle plane of the models. Note that PD images are displayed on a smaller dynamic range.

of the transmitted waves was empirically chosen at 0.12 to produce high-SNR images.

D. Data Processing

All the data were processed offline on a workstation equipped with an Intel Xeon E6-2630 central processing unit (Intel Corporation, Santa Clara, CA, USA), 64-GB DDR3 RAM, and an Nvidia Titan XP graphics processing unit (GPU-NVidia Corporation, Santa Clara, CA, USA). ASAP and PD images were produced from the same RF signals with the methods described in Section II-A. Coherent compounding was performed to generate the B-mode images from the full aperture (PD) and two subapertures (ASAP) from the RF data. To ease the processing burden of HFR imaging, the DAS beamformer was executed using a GPU developed in-house for real-time image reconstruction. The respiratory motion was estimated by applying principle component analysis (PCA) on small patches corresponding to the region of interest (e.g., tumor and kidney) [29]. Any motion-affected frames were rejected before clutter filtering to avoid artifacts from respiratory motion. Adaptive SVD clutter filtering was then performed to remove the clutter. This was done by automatic detection of the turning point on the energy curve derived from the singular value and removing all the lower subspace before the turning point, as previously described in [23]. For each imaging slice, ASAP and PD vascular images were generated with the methods, as shown in Fig. 1. The final volumetric image was formed by stacking the 2-D images. Volume rendering was accomplished in ParaView.

To evaluate the image quality, we compared the ASAP images with the PD images using two metrics, similar to [26].

The SNR and the contrast-to-noise ratio (CNR) were evaluated as follows:

$$\text{SNR} = 10\log_{10}\left(\frac{\mu_s}{\mu_n}\right) \tag{4}$$

$$\text{CNR} = 10\log_{10}\left(\frac{|\mu_s - \mu_n|}{\sqrt{\sigma_s^2 - \sigma_n^2}}\right) \tag{5}$$

where μ_s and μ_n are the mean value of the signal and noise regions, respectively, and σ_s and σ_n are the standard deviation of the pixel values in these regions.

III. RESULTS

Fig. 3 shows the comparison between the B-mode, PD, and ASAP images of a mouse kidney, a liver, and a tumor. The vasculature is not visible in the B-mode images due to the relatively high amplitude clutter signal in comparison to the blood signal. Such strong clutter signal can be greatly suppressed and the signals from the blood cells are sufficiently strong to reveal the vasculature after using SVD filter and PD processing. However, there is still significant noise background in the PD images that reduces the contrast of the vessel signals. The background noise, which is amplified with the imaging depth due to the application of depth-gain compensation, further compromised the visibility of the smaller vessels at the deeper region. The ASAP technique, on the other hand, can substantially reduce the background noise in comparison to the PD images, to detect the weak blood cell signals from microvessels and produce high contrast vascular images, as shown in Fig. 3 (right column).
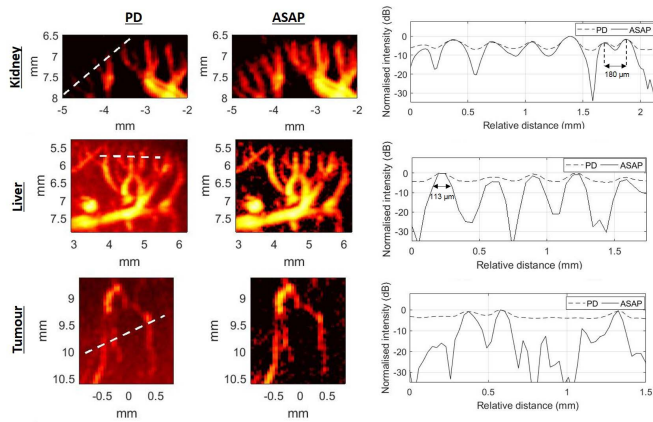
Fig. 4. Magnified images and their corresponding intensity profiles of the kidney (top row), liver (middle row), and tumor model (bottom row) showing the improved visibility of small vessels seen in the ASAP images in comparison to the PD images. The intensity profiles are extracted from the lines marked on the PD images. Note that the PD and ASAP images are displayed at 20- and 30-dB dynamic range, respectively.

The image quality improvement is further illustrated by selecting a few regions of interest (white boxes) from Fig. 3 and magnified in Fig. 4. The microvessels are submerged by noise in the PD images but are clearly discernible in the ASAP images. From the intensity profile, it is also evident that the background noise in the ASAP images is significantly reduced, producing a spike-shaped profile with lower noise floor, whereas relatively flat profiles are observed for the PD images. It should be noted that while the noise is reduced, the image resolution is maintained where microvessel as small as 113 μm in full-width at half-maximum (FWHM) was visualized and two microvessels with 180 μm apart were well separated.

Fig. 5 shows more examples of the vasculature images acquired at different slices. Vasculature that is barely seen in the PD images can be clearly visualized in the ASAP images (blue arrows shown in Fig. 5). To quantify the SNR and CNR improvement, signal regions (white boxes in shown Fig. 5) and noise regions (green boxes) were manually selected from both PD and ASAP images, and results are reported in Table I. ASAP is demonstrated to improve the SNR by an average of 10 dB in comparison to PD whereas marginal differences were found for the CNR.

Fig. 6 shows the flow velocity mapping of the vasculatures estimated using phase information extracted from lag-1 autocorrelation and amplitude thresholding using the power signal of the ASAP. Functional information such as the flow direction and blood velocity are clearly visualized.

Fig. 7 demonstrates the volumetric vasculature images of the mouse kidney, liver, and tumor. The rotation of the 3-D images along the x–z plane can be found in Movies 1–6. All the 2-D images acquired were stacked accordingly and rendered in 3-D with a constant slice thickness equivalent to the motor step size. Morphological and functional differences are readily apparent between the nontumor models (kidney and liver) and tumor. The microvessel structures of the mouse kidney and liver are relatively more homogenous, organized, and emanating from larger vessels in the medullary region, and
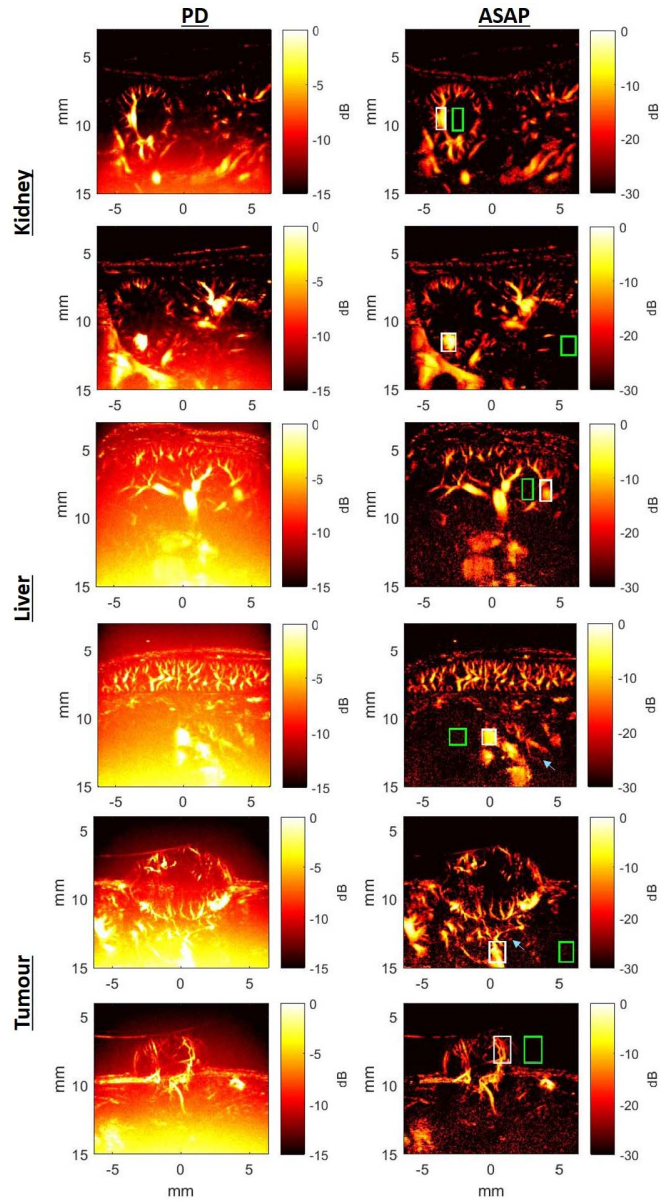

Fig. 5. More examples of the vascular images collected at different slice positions within the volumetric data set and processed using PD and ASAP. The white and green boxes are manually selected to quantify the SNR and CNR, respectively. The blue arrows show the vasculatures that are barely seen on PD images but clearly visible on ASAP images. Note: PD images are displayed on a smaller dynamic range.

tend to have straight sections, whereas the tumor vasculature is more tortuous and chaotic, with a more vascularized outer rim and relatively avascular central region. The functional images with directional velocity mappings further illustrated the homogeneity of blood flow in tumor when compared to the nontumor kidney and liver. Note that some artifacts exist in the images. These are mainly due to inefficiency of the clutter filtering, which was not able to completely remove the effects of respiration motion, particularly in the case of the kidney and liver.

IV. DISCUSSION

In this study, we presented a technique for 3-D HFR noncontrast enhanced vascular imaging using a linear array
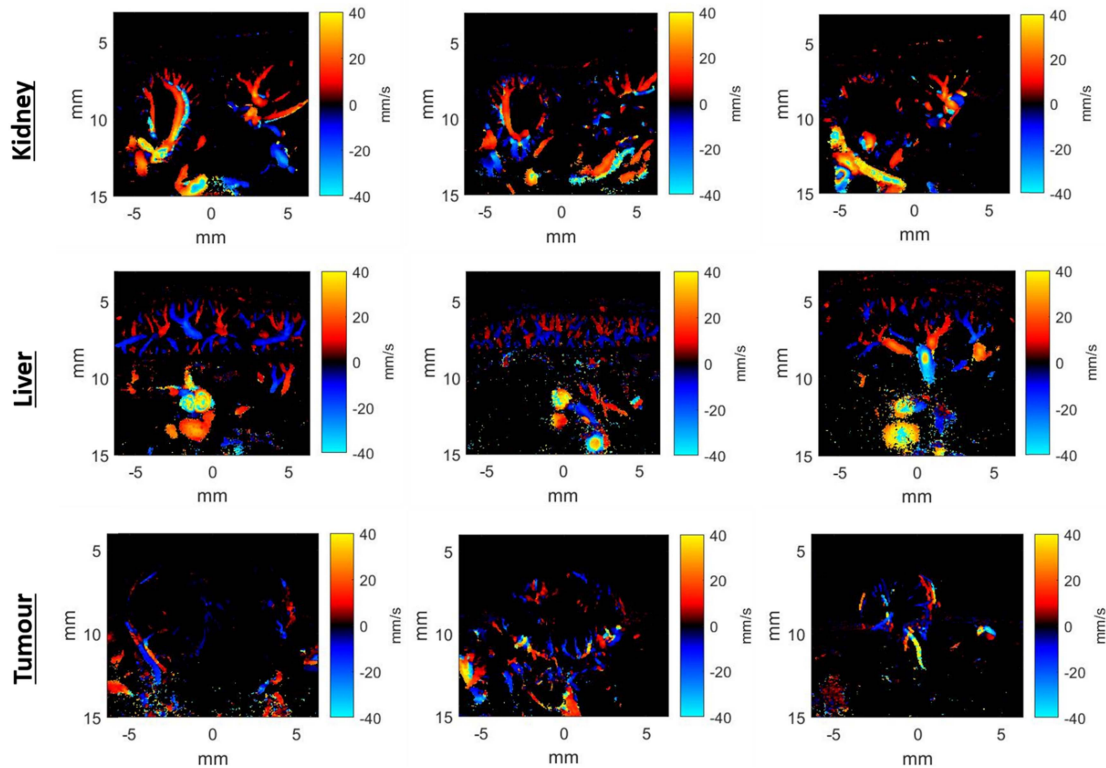
Fig. 6. Directional velocity mapping of the vascular images collected at different slice positions within the volumetric data set and processed using lag-1 autocorrelation in combination with the ASAP. Note: Red and blue indicate the flow direction toward and away from the transducer surface assuming the Doppler pulse propagated perpendicular to the transducer surface.

TABLE I
COMPARISON OF THE SNR AND CNR OF THE PD AND ASAP

Image	SNR		CNR	
	PD	ASAP	PD	ASAP
K-1	4.60	13.30	0.68	0.25
K-2	7.65	19.29	2.01	2.75
L-1	1.35	8.20	0.12	1.18
L-2	3.11	11.17	3.37	3.90
T-1	2.52	11.54	0.05	0.12
T-2	2.03	9.59	0.18	0.22
Average	3.54±2.09	12.18±3.55	1.06±1.22	1.40±1.44

K = Kidney, L = Liver, T = Tumour, PD= Power Doppler, ASAP= Acoustic Sub-aperture processing

transducer and computer-controlled translational stage. This is the first demonstration of ASAP for microvascular volumetric imaging without contrast agents. The initial quantitative evaluations were performed on nontumor models (mouse kidney and liver) and a tumor model (subcutaneous xenograft), and the results indicated superior vasculature images with an average of 10-dB contrast improvement over the existing ultrafast PD technique. Such a 3-D microvascular imaging tool with significantly enhanced image quality, and without the need of contrast agent injection, has potential to be applied to a wide range of applications, including the screening and early detection of cancer and diseases impacting microvasculature, regular longitudinal monitoring of therapies, and improved brain functional ultrasound imaging.

The high contrast and improved visibility of the vasculature using ASAP in comparison with PD are shown in Figs. 3–5. Such a substantial noise reduction enhances the ability to distinguish small vessels from the noise background and subsequently produce a high-quality volumetric vasculature image, as shown in Fig. 7. While ASAP helps in segmentation of blood vessels, functional information can be extracted by combining ASAP and lag-1 autocorrelation to map the flow direction and velocity, as shown in Figs. 6 and 7. The qualitative assessment revealed morphology and functional differences between the nontumor and tumor model.

ASAP processing can be applied to improve the visualization of microvasculature with and without contrast agents. The differences between the ASAP images acquired without and with contrast agents are shown in Fig. 8. Noncontrast images were acquired at MI of 0.12, whereas the contrast-enhanced images were acquired after the bolus injection of diluted home-made microbubbles (10^6 microbubbles/mL) at an MI of 0.05. Images were acquired under similar settings except that the lower MI was used to avoid microbubbles' destruction after microbubbles injection. The SNRs quantified from the ASAP images, with and without contrast agents, are 10.71 and 9.46 dB, respectively. Despite the marginal difference in the SNR of the noncontrast- and contrast-enhanced images, were found between these SNRs, more microvessels can be seen in the latter (indicated by the white arrows),
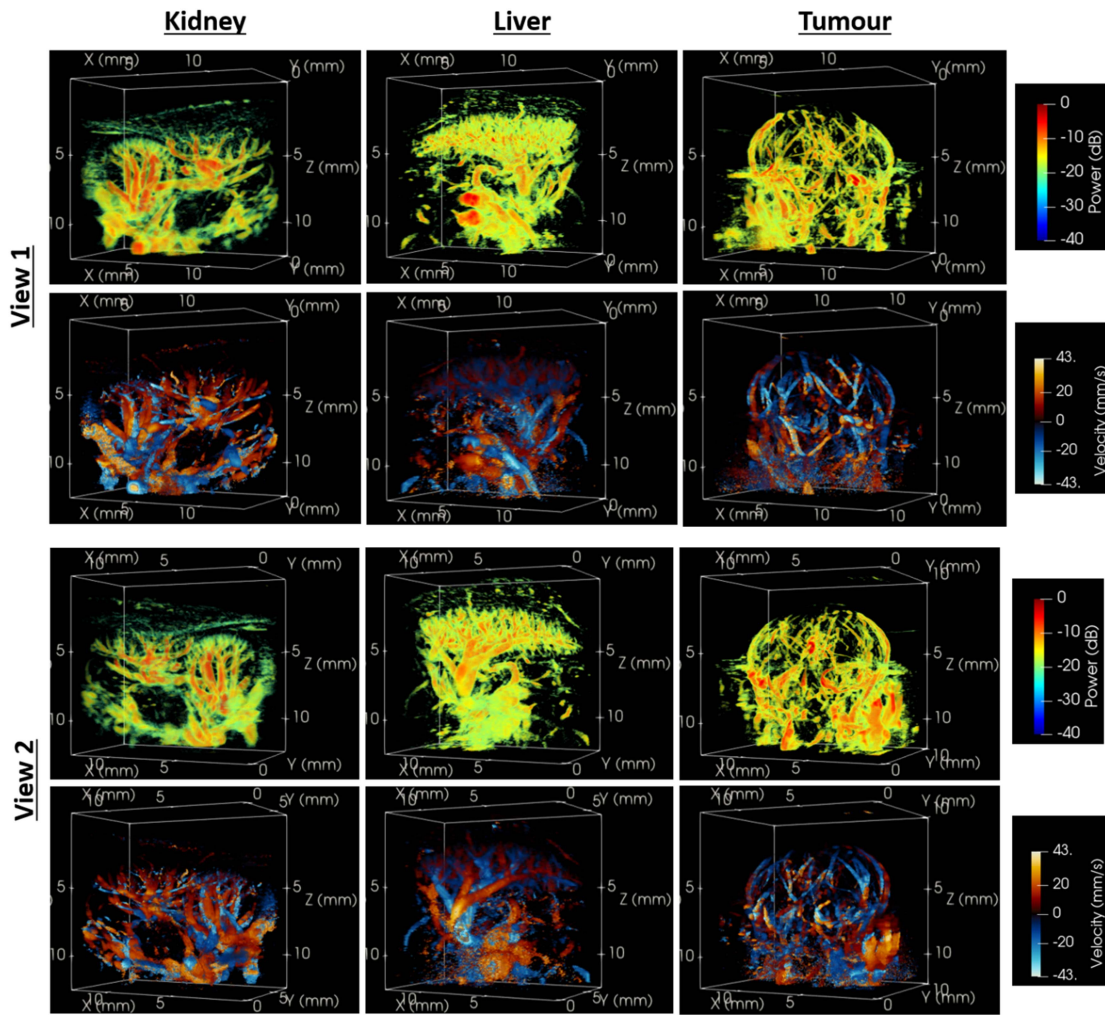
Fig. 7. Volume rendered presentations of 3-D microvascular images of a nontumor kidney (left), liver (middle), and tumor (right) mouse model visualized from two different viewpoints. Volumetric data sets are generated by stacking multiple 2-D high-contrast microvascular images processed using ASAP. The power signal was color coded for the microvascular images in the first and third rows whereas the directional velocity extracted from the lag-1 autocorrelation in combination with the ASAP were displayed in the second and fourth rows.
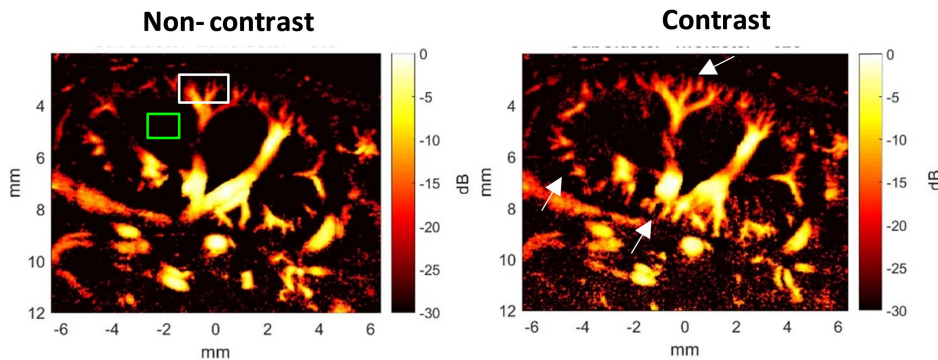

Fig. 8. Comparison between the microvasculature image generated using ASAP before (left) and after the injection of microbubbles (right). More microvessels can be seen after the contrast injection as indicated by the white arrows. Note: White and green boxes are used to evaluate the SNR.

even at the high-frequency circumstance, where blood is known to resonate more than microbubbles. Further investigations are needed to compare the performance of noncontrast- and contrast-enhanced microvascular imaging at lower frequencies.

Volumetric microvascular imaging has been previously demonstrated using other ultrasound techniques.

Demené *et al.* [30] demonstrated a 4-D microvascular imaging based on ultrafast Doppler tomography on rats' brain. A 1-D-array transducer mounted on a 4 degree of freedom (three translation plus one rotation) mechanical stage was used to acquire two volumetric measurements of the same object by translating the probe in the probe's elevation direction and rotating the probe along the center plane.

Flow information from the two volumes was extracted using ultrafast Doppler and fused using a deconvolution technique to form a final volume with an isotropic resolution. Such an image acquisition strategy, although computational demanding, can also be used to enhance our technique to achieve an isotropic resolved volumetric images. Gessner *et al.* [11] developed a technique known as acoustic angiography for contrast imaging. Although high-resolution image was achieved, this technique requires a customized dual-frequency transducer to emit pulse for microbubble excitation at low frequency (2–4 MHz) and confocally detect ultraharmonic echoes at 15–45-MHz bandwidth. Our technique, on the other hand, does not require the injection of microbubbles and can be readily translated for clinical applications using any lower frequency transducers with or without contrast injection. The ultrasound super-resolution or ultrasound super-localization microscopy is another technique developed to resolve microvascular imaging beyond ultrasound diffraction limit. The 3-D super-resolution imaging was demonstrated using a linear array and a controlled stage [6], using two parallel probes [31], [32] or a 3-D hemispherical ultrasonic array [33]. With the first approach, tracking is not possible in the elevation direction; therefore, vessel in the elevation direction is projected in plane and can be blurred. The latter two approaches attempted to solve the problem and achieve an isotropic super resolution. Despite achieving very high resolution and SNR, super-resolution technique requires relatively long acquisition time to accumulate localization signals and to ensure the final reconstructed images depict the real vasculature rather than a very small fraction of the microvessels. Our technique, in contrast, can be implemented in real-time and may remain a better approach for microvascular imaging applications, where super-resolved pixels beyond diffraction limit is not required. This may potentially provide a first-line diagnosis and treatment, where real-time monitoring is needed.

From the practical standpoint, real-time processing of the 3-D vascular images is possible by harnessing the parallel processing of GPUs. Although the memory required to store the beamformed images from the two subapertures and the SVD clutter filtering operation is twice as much as that needed for PD processing, the computational complexity of the ASAP is actually equivalent to the PD. If M is the number of channels and N is number of pixels in depth for each channel, the computational complexities of a DAS beamformer and SVD processing are $O(M^2 N)$ and $O(MN^2)$, respectively. The correlation estimator and phase suppressor, which have the complexity of $O(MN)$, will not affect the final computation time. To further reduce the computation time for real-time realization, beamforming can be implemented in the Fourier domain [34] with the complexity of $O(MN \log(MN))$, and the SVD clutter filter can be changed to a polynomial regression filter with much lower complexity.

While volumetric images can be acquired using a 2-D imaging system and a linear translational stage, the long acquisition time could limit the practicality of volumetric imaging. Given that the acquisition time for each scanning plane was 1.5 s, and the data-saving time was 10 s, a complete 3-D scan of a 1-cm
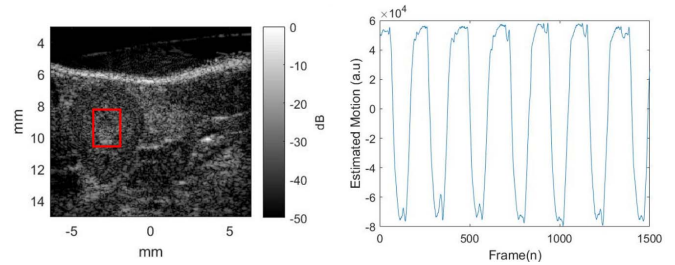

Fig. 9.　Respiratory motion estimated using PCA from the HFR images. Note: Motion (right) was extracted from the region bounded by the red box drawn on the B-mode image (left).

region of interest required an imaging time of nearly 13 min for a step size of 150 μm. However, the imaging time can be reduced to less than 2 min with a much efficient data-saving procedure or a real-time processing pipeline without the need to save the prebeamformed channel data. With a matrix array plane-wave volumetric data acquisition, such limitations can be avoided.

The respiratory motion could potentially blur the final reconstructed vascular images. It also limits the effectiveness of the clutter filter which assumes that the tissue is nearly stationary. Despite having the respiratory motion estimated using the PCA analysis as shown in Fig. 9, there exists some residual motion due to the nonstationary tissue motion even when more than 50% of the frames were discarded. This explained the residual clutter artifacts that appeared on the both the 2-D and 3-D vasculature images. In order to alleviate the effects of respiratory motion, motion correction to register the images before the application of clutter filtering will be implemented in the future.

Another limitation lies in the use of 2-D ultrasound for imaging 3-D structures. The ultrasound field in the elevation direction is nonuniform, making it challenging to detect vessels oriented in the elevation plane, and the reduced image resolution in the elevation plane makes it difficult to distinguish elevationally adjacent vessels. As we assume that the elevation thickness is equivalent to the scanning step size, this is likely to limit sensitivity and resolution to detecting only microvessels appear to be 150 μm or larger in this study. This is an inherent limitation of 2-D imaging and may be well resolved using a matrix ultrasound transducer or imaging strategies which could enhance the elevation resolution.

V. Conclusion

We demonstrated that the ASAP technique can be used *in vivo* without microbubble contrast agent to generate 3-D microvascular images using 2-D HFR ultrasound and a computer-controlled translation stage. In comparison to the existing PD imaging, the high contrast volumetric images generated using ASAP can facilitate improved microvascular visualization and quantification, and hold the promise for clinical applications.

References

[1] T. Jeswani and A. R. Padhani, "Imaging tumour angiogenesis," *Cancer Imag.*, vol. 5, no. 1, pp. 131–138, Dec. 2005.

[2] K. W. Ferrara, C. R. Merritt, P. N. Burns, F. S. Foster, R. F. Mattrey, and S. A. Wickline, "Evaluation of tumor angiogenesis with US: Imaging, Doppler, and contrast agents," *Acad. Radiol.*, vol. 7, no. 10, pp. 824–839, 2000.

[3] N. Weidner *et al.*, "Tumor angiogenesis: A new significant and independent prognostic indicator in early-stage breast carcinoma," *J. Nat. Cancer Inst.*, vol. 84, no. 24, pp. 1875–1887, Dec. 1992.

[4] C. Kasai, K. Namekawa, A. Koyano, and R. Omoto, "Real-time two-dimensional blood flow imaging using an autocorrelation technique," *IEEE Trans. Sonics Ultrason.*, vol. 32, no. 3, pp. 458–464, May 1985.

[5] T. Loupas, J. T. Powers, and R. W. Gill, "An axial velocity estimator for ultrasound blood flow imaging, based on a full evaluation of the Doppler equation by means of a two-dimensional autocorrelation approach," *IEEE Trans. Ultrason., Ferroelectr., Freq. Control*, vol. 42, no. 4, pp. 672–688, Jul. 1995.

[6] F. Lin, S. E. Shelton, D. Espíndola, J. D. Rojas, G. Pinton, and P. A. Dayton, "3-D Ultrasound localization microscopy for identifying microvascular morphology features of tumor angiogenesis at a resolution beyond the diffraction limit of conventional ultrasound," *Theranostics*, vol. 7, no. 1, pp. 196–204, Jan. 2017.

[7] R. J. Eckersley, C. T. Chin, and P. N. Burns, "Optimising phase and amplitude modulation schemes for imaging microbubble contrast agents at low acoustic power," *Ultrasound Med. Biol.*, vol. 31, no. 2, pp. 213–219, Feb. 2005.

[8] J. M. Borsboom, C. T. Chin, and N. de Jong, "Nonlinear coded excitation method for ultrasound contrast imaging," *Ultrasound Med. Biol.*, vol. 29, no. 2, pp. 277–284, Feb. 2003.

[9] A. Bouakaz, S. Frigstad, F. J. T. Cate, and N. de Jong, "Super harmonic imaging: A new imaging technique for improved contrast detection," *Ultrasound Med. Biol.*, vol. 28, no. 1, pp. 59–68, Jan. 2002.

[10] D. H. Simpson, C. T. Chin, and P. N. Burns, "Pulse inversion Doppler: A new method for detecting nonlinear echoes from microbubble contrast agents," *IEEE Trans. Ultrason., Ferroelectr., Freq. Control*, vol. 46, no. 2, pp. 372–382, Mar. 1999.

[11] R. C. Gessner, C. B. Frederick, F. S. Foster, and P. A. Dayton, "Acoustic angiography: A new imaging modality for assessing microvasculature architecture," *J. Biomed. Imag.*, vol. 2013, p. 14, Jan. 2013.

[12] K. Christensen-Jeffries, R. J. Browning, M.-X. Tang, C. Dunsby, and R. J. Eckersley, "In vivo acoustic super-resolution and super-resolved velocity mapping using microbubbles," *IEEE Trans. Med. Imag.*, vol. 34, no. 2, pp. 433–440, Feb. 2015.

[13] C. Errico *et al.*, "Ultrafast ultrasound localization microscopy for deep super-resolution vascular imaging," *Nature*, vol. 527, no. 7579, pp. 499–502, Nov. 2015.

[14] J. Bercoff *et al.*, "Ultrafast compound Doppler imaging: Providing full blood flow characterization," *IEEE Trans. Ultrason., Ferroelectr., Freq. Control*, vol. 58, no. 1, pp. 134–147, Jan. 2011.

[15] J. Jensen, S. Nikolov, C. H. Alfred, and D. Garcia, "Ultrasound vector flow imaging—Part II: Parallel systems," *IEEE Trans. Ultrason., Ferroelectr., Freq. Control*, vol. 63, no. 11, pp. 1722–1732, Nov. 2016.

[16] C. H. Leow, E. Bazigou, R. J. Eckersley, A. C. Yu, P. D. Weinberg, and M. X. Tang, "Flow velocity mapping using contrast enhanced high-frame-rate plane wave ultrasound and image tracking: Methods and initial *in vitro* and *in vivo* evaluation," vol. 41, no. 11, pp. 2913–2925, 2015.

[17] C. H. Leow and M.-X. Tang, "Spatio-temporal flow and wall shear stress mapping based on incoherent ensemble-correlation of ultrafast contrast enhanced ultrasound images," *Ultrasound Med. Biol.*, vol. 44, no. 1, pp. 134–152, Jan. 2018.

[18] M. E. G. Toulemonde *et al.*, "High frame-rate contrast echocardiography: In-human demonstration," *JACC Cardiovascular Imag.*, vol. 11, no. 6, pp. 923–924, 2018.

[19] C. C. Chang, P. Y. Chen, H. Huang, and C. C. Huang, "*In vivo* visualization of vasculature in adult zebrafish by high frequency ultrafast ultrasound imaging," *IEEE Trans. Biomed. Eng.*, to be published.

[20] C. Tremblay-Darveau, R. Williams, L. Milot, M. Bruce, and P. N. Burns, "Combined perfusion and Doppler imaging using plane-wave nonlinear detection and microbubble contrast agents," *IEEE Trans. Ultrason., Ferroelectr., Freq. Control*, vol. 61, no. 12, pp. 1988–2000, Dec. 2014.

[21] A. C. H. Yu and L. Lovstakken, "Eigen-based clutter filter design for ultrasound color flow imaging: A review," *IEEE Trans. Ultrason., Ferroelectr., Freq. Control*, vol. 57, no. 5, pp. 1096–1111, May 2010.

[22] C. Demené *et al.*, "Spatiotemporal clutter filtering of ultrafast ultrasound data highly increases Doppler and fultrasound sensitivity," *IEEE Trans. Med. Imag.*, vol. 34, no. 11, pp. 2271–2285, Nov. 2015.

[23] P. Song, A. Manduca, J. D. Trzasko, and S. Chen, "Ultrasound small vessel imaging with block-wise adaptive local clutter filtering," *IEEE Trans. Med. Imag.*, vol. 36, no. 1, pp. 251–262, Jan. 2017.

[24] C. Tremblay-Darveau *et al.*, "Improved contrast-enhanced power Doppler using a coherence-based estimator," *IEEE Trans. Med. Imag.*, vol. 36, no. 9, p. 1901–1911, Sep. 2017.

[25] Y. L. Li and J. J. Dahl, "Coherent flow power Doppler (CFPD): Flow detection using spatial coherence beamforming," *IEEE Trans. Ultrason., Ferroelectr., Freq. Control*, vol. 62, no. 6, pp. 1022–1035, Jun. 2015.

[26] A. Stanziola, C. H. Leow, E. Bazigou, P. D. Weinberg, and M.-X. Tang, "ASAP: Super-contrast vasculature imaging using coherence analysis and high frame-rate contrast enhanced ultrasound," *IEEE Trans. Med. Imag.*, vol. 37, no. 8, pp. 1847–1856, Aug. 2018.

[27] A. Stanziola and M.-X. Tang, "Super contrast imaging using high frame-rate CEUS and spatial and temporal signal processing," in *Proc. 22nd Eur. Symp. Ultrasound Contrast Imag.*, Jan. 2017, p. B7.

[28] C. H. Seo and J. T. Yen, "Sidelobe suppression in ultrasound imaging using dual apodization with cross-correlation," *IEEE Trans. Ultrason., Ferroelectr., Freq. Control*, vol. 55, no. 10, pp. 2198–2210, Oct. 2008.

[29] U. Wijenayake and S.-Y. Park, "Real-time external respiratory motion measuring technique using an RGB-D camera and principal component analysis," *Sensors*, vol. 17, no. 8, p. 1840, Aug. 2017.

[30] C. Demené *et al.*, "4D microvascular imaging based on ultrafast Doppler tomography," *NeuroImage*, vol. 127, pp. 472–483, Feb. 2016.

[31] K. Christensen-Jeffries, J. Brown, P. Aljabar, M. Tang, C. Dunsby, and R. J. Eckersley, "3-D *in vitro* acoustic super-resolution and super-resolved velocity mapping using microbubbles," *IEEE Trans. Ultrason., Ferroelectr., Freq. Control*, vol. 64, no. 10, pp. 1478–1486, Oct. 2017.

[32] Y. Desailly, O. Couture, M. Fink, and M. Tanter, "Sono-activated ultrasound localization microscopy," *Appl. Phys. Lett.*, vol. 103, no. 17, Oct. 2013, Art. no. 174107.

[33] M. A. O'Reilly and K. Hynynen, "A super-resolution ultrasound method for brain vascular mapping," *Med. Phys.*, vol. 40, no. 11, Nov. 2013, Art. no. 110701.

[34] J.-Y. Lu, "2-D and 3-D high frame rate imaging with limited diffraction beams," *IEEE Trans. Ultrason., Ferroelectr., Freq. Control*, vol. 44, no. 4, pp. 839–856, Jul. 1997.

Chee Hau Leow received the Ph.D. degree in bioengineering from Imperial College London, London, U.K., in 2016.

He is currently a Research Associate with the Department of Bioengineering, Imperial College London. His research interests include parallel processing for ultrafast ultrasound image reconstruction and quantitative analysis for cancer and cardiovascular applications.

Nigel L. Bush, photograph and biography not available at the time of publication.
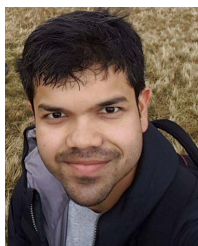
Antonio Stanziola received the Ph.D. degree in bioengineering from Imperial College London, London, U.K., with a dissertation in ultrasound beamforming for vascular imaging.

His current research interests are ultrasound image reconstruction, statistical signal processing, and ultrasound contrast imaging.

Marta Braga received the B.Sc. degree in biomedical engineering and the M.Sc. degree in imaging and radiation from the University of Coimbra, Coimbra, Portugal, in 2012, and the Ph.D. degree from the Imperial College London, London, U.K., in 2019.

She is currently a Research Associate with the Department of Surgery and Cancer, Imperial College London. Her research interests include molecular imaging of cancer with PET and ultrasound.

Eric O. Aboagye is currently a Professor of Cancer Pharmacology and Molecular Imaging and the Director of the CRUK–EPSRC–MRC–NIHR Comprehensive Cancer Imaging Centre, London, U.K. His group is interested in the discovery and development of new methods for experimental and clinical cancer molecular imaging. In the past 5 years, the team has invented and translated three novel cancer diagnostics into human application.

Anant Shah received the Ph.D. degree in biophysics from The Institute of Cancer Research, London, U.K., in 2014, with a focus on photoacoustic imaging of molecular markers of cancer prognosis and response using gold nanoparticles.

He is currently a Higher Research Scientist with the Ultrasound and Underwater Acoustics, National Physical Laboratory, Teddington, U.K. His research is oriented toward photoacoustic imaging, photoacoustic microscopy, and acoustic characterization of ultrasound fields and materials.

Jeffrey C. Bamber is currently a Professor of physics applied to medicine, the Leader of the Ultrasound and Optical Imaging Team, and the Deputy Dean of Biomedical Sciences with The Institute of Cancer Research London, London, U.K. He holds honorary appointments at The Royal Marsden Hospital, London, and other hospitals and colleges in London. His research aims to increase ultrasound's quantitative, functional, and molecular imaging capability, providing tools to experimental cancer biology and helping to improve cancer treatment by bringing ultrasound-based methods to clinical problems such as early diagnosis, assessing tumor aggressiveness and response, and guiding treatment.

Prof. Bamber is past President of the International Association for Breast Ultrasound and past Vice-President of the International Society of Skin Imaging. He is Vice-President of the IBUS Breast Imaging School.

Javier Hernández-Gil, photograph and biography not available at the time of publication.

Nicholas J. Long is currently the Sir Edward Frankland Endowed Chair Professor of inorganic chemistry with Imperial College London, London, U.K. He has made significant impact within the area of biomedical imaging and is a leader in synthetic imaging chemistry and probe design. Recent innovations include the development of a novel dual-modal magnetic resonance imaging (MRI)/fluorescence probe that senses zinc, the first example of an MRI contrast agent that can target formyl peptide receptors (FPR1), utilizing smart and targeted nanoparticles for cancer imaging, and new [11C] and [18F] PET radiolabeling technology, companies such as GSK are using his probes for cardiovascular imaging.

Meng-Xing Tang (M'05–SM'17) is currently a Professor/Chair of biomedical imaging with the Department of Bioengineering, Imperial College London, London, U.K., where he leads the Ultrasound Laboratory for Imaging and Sensing (ULIS). He has authored more than 90 peer-reviewed journal papers. His current research mainly focuses on developing and applying new imaging techniques, particularly of ultrahigh temporal and spatial resolution using ultrasound, contrast agents, and computing.

Prof. Tang is an Associate Editor of the IEEE TRANSACTIONS ON ULTRASONICS, FERROELECTRICS, AND FREQUENCY CONTROL.